Simulation-Based Design and Experimental Evaluation of a Spatially Controllable CVD Reactor

Jae-Ouk Choo and Raymond A. Adomaitis
Dept. of Chemical Engineering and Institute for Systems Research, University of Maryland, College Park, MD 20742

Gary W. Rubloff, Laurent Henn-Lecordier, and Yijun Liu
Dept. of Materials Science and Engineering and Institute for Systems Research, University of Maryland, College Park, MD 20742

DOI 10.1002/aic.10358
Published online in Wiley InterScience (www.interscience.wiley.com).

Most conventional chemical vapor deposition (CVD) systems do not have the spatial actuation and sensing capabilities necessary to control deposition uniformity, or to intentionally induce nonuniform deposition patterns for single-wafer combinatorial CVD experiments. In an effort to address these limitations, a novel CVD reactor system has been developed that can explicitly control the spatial profile of gas-phase chemical composition across the wafer surface. This paper discusses the simulation-based design of a prototype reactor system and the results of preliminary experiments performed to evaluate the performance of the prototype in depositing tungsten films. Initial experimental results demonstrate that it is possible to produce spatially patterned wafers using a CVD process by controlling gas-phase reactant composition, opening the door to a new class of flexible and highly controllable CVD reactor designs. © 2005 American Institute of Chemical Engineers *AIChE J,* 51: 572–584, 2005
Keywords: semiconductor processing, chemical vapor deposition, distributed parameter systems, simulation

Introduction

Chemical vapor deposition (CVD) is one of the essential unit operations in semiconductor manufacturing because of its ability to deposit thin, smooth films conformally onto submicron-scale features. CVD processes have evolved together with the semiconductor industry, from early bell-jar CVD reactors to current cold-wall single-wafer reactors (Xia et al., 2000). The continuing reduction of device feature size, growing scale of device integration, expanding number of new electronic materials, and increasing substrate (wafer) size motivate development of the new CVD processes necessary to sustain the advancement of microelectronic technology. However, current equipment designs are aimed at specific deposition processes and operating conditions (such as pressures, chemical species, flows, temperatures) with the design goal of producing process uniformity across large wafers (300 mm diameter, resulting in hundreds of semiconductor chips) at the nominal design conditions. Optimizing a design to CVD and other manufacturing equipment for a specific range of design conditions has a number of fundamental shortcomings:

(1) Semiconductor manufacturing processes change rapidly in time (relative to typical petrochemical processes). Because technology improvements must be implemented incrementally to maintain or improve yields in complex, multistep wafer production sequences, a new generation of process equipment technology may emerge only after several of these improvement steps.

Y. Liu is currently at ASM International, 3440 East University Drive, Phoenix, AZ 85034-7200.
Correspondence concerning this article should be addressed to R. A. Adomaitis at adomaiti@umd.edu.

(2) Process conditions for optimal material and device quality often do not meet the across-wafer uniformity requirements for manufacturing, forcing a trade-off between product performance and manufacturing productivity.

(3) Fundamental chemical and physical mechanisms for semiconductor processes are often not well known, so that it is difficult to identify *a priori* the best design that balances the demands of product performance and manufacturing uniformity.

(4) Experimentation for process optimization is expensive, requiring sets of runs to investigate and characterize complex process behavior.

Equipment design for uniformity

Current CVD reactor designs typically consist of a cooled-wall reaction (vacuum) chamber in which one to several wafers are processed. The energy needed to drive the deposition reactions is provided by an inductively heated susceptor or a wafer stage heated by external lamps or electrical resistance heating. Reactant gases enter the reaction chamber through a gas delivery system, flow over the wafer(s), and the residual gas is pumped out through the chamber exhaust port. Because of the importance of spatially uniform (across-wafer) processing capabilities, showerhead designs for gas delivery to the wafer typically incorporate a high density of uniformly spaced small holes in an attempt to distribute gas flow as uniformly as possible across a large-diameter wafer. In addition, reactor design components including chamber, wafer position (and rotation), pumping, heating, and gas inlet are commonly structured to achieve high uniformity with cylindrical symmetry about the wafer.

Significant research effort has been directed toward improving growth uniformity of CVD process. Early experimental and simulation-based process equipment research focused on developing an understanding of the important transport and reaction mechanisms of CVD processes and devising optimization methods to aid process parameter selection. For example, Wang et al. (1986) used flow visualization techniques to show that heated wafers can disturb gas flow patterns; their experiments suggested lowering operation pressures to reduce the perturbation. Moffat and Jensen (1988) demonstrated the utility of simulation technology for process optimization in the context of a horizontal Si homoepitaxial deposition reactor. Their simulation study examined the relationship between the growth uniformity and tilt angle of the susceptor, giving the optimal setting for this reactor geometry parameter. Another example of rigorous modeling and simulation was performed by Kleijn et al. (1989). Their mathematical model was used to show the significance of thermal diffusion and its effect on growth uniformity and gas-phase reactant species distribution.

The evolution of CVD reactor designs also has been motivated by the need to improve growth uniformity. For example, various showerhead designs have been developed to generate uniform gas flow patterns over the wafer surface (Gadgil, 1993; Wang et al., 1986) or to produce uniform film deposition rates (Kim and Lee, 1997; Kobayashi et al., 1997). Still more advanced design features are found in the annular, three-zone Texas Instruments (TI) showerhead (Moslehi et al., 1995) for tungsten (W) and other CVD processes, where individual gas mass flow controllers could be used to set the gas flow rate to each segment.

In some metal organic chemical vapor deposition (MOCVD) processes, the separation of gas precursors is critical because highly reactive gas precursors can cause undesirable gas-phase reactions. In an effort to reduce gas-phase reactions, Van der Stricht et al. (1997) developed a vertical reactor with separate feed ports for each precursor species, and experiments revealed the relationship between the wafer rotation rate and thickness uniformity of GaN and InGaN films. Another example of using separate gas injectors for individual precursors can be found in the horizontal flow MOCVD reactor introduced by Yang et al. (1999). Theodoropoulos et al. (2000) described a new MOCVD reactor design of featuring an annular-ring showerhead configuration that allowed the controlled injection of separate precursors. Several annular ring designs were evaluated in that study, and as with Van der Stricht and Yang, Theodoropoulos and coworkers concluded that novel gas delivery designs offered new operational degrees of freedom with which uniformity could be controlled; they also pointed to the importance of simulation tools in selecting optimized operating conditions.

CVD reactor designs have been developed specifically to allow or improve active control of wafer processing conditions during the dynamic processing cycle. For example, work at TI (Moslehi et al., 1992) exploited multiple (three and four) heating zones radially across the wafer in single-wafer rapid thermal processing to achieve temperature uniformity. That approach has been incorporated into commercial rapid thermal processor (RTP) equipment (such as from CVC Products and from Applied Materials). The SEMATECH test-bed RTP system (Stuber et al., 1998) and the three-zone RTP system at North Carolina State University (NCSU) (Kiether et al., 1994) exploit independent lamp zones for edge-cooling compensation and dynamic uniformity control. Further developments in this area include reduced-model–based real-time control studies of the three-zone NCSU RTP system (Christofides, 2001; Theodoropoulou et al., 1999) and reduced-model–based order state estimation and optimal control of a horizontal high-pressure CVD system (Banks et al., 2002; Kepler et al., 2000, 2001).

The programmable reactor concept

The existing design strategy of semiconductor CVD manufacturing equipment faces fundamental barriers limiting the development of next-generation reactor systems; there is a need for a new design paradigm to: (1) decouple fundamental materials and product quality requirements from across-wafer uniformity in manufacturing, so that both may be achieved simultaneously; (2) accelerate materials and process learning and optimization; and (3) develop equipment that is flexible and scalable to succeeding generations of the technology.

As a response to these perceived CVD reactor design shortcomings, this paper presents the development of a novel CVD reactor intended to improve across-wafer two-dimensional controllability. This new CVD reactor introduces a segmented showerhead design featuring individually controllable gas distribution actuators, a design that reverses the residual gas flow by directing it up through the showerhead, and sampling ports for in situ gas sampling (Figure 1). Herein we describe the

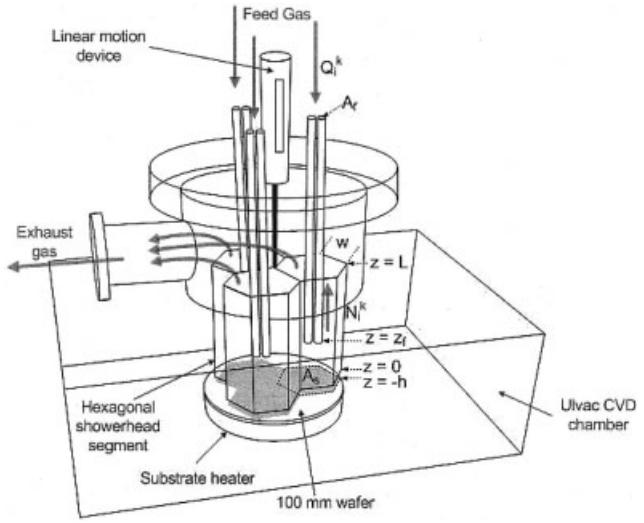

Figure 1. Programmable CVD reactor three-zone prototype.

The segmented showerhead structure, segment feed and sampling lines, linear motion device, and notation used in developing the simulator are shown.

development of this novel design concept by simulation, a sequence of experiments performed using a prototype reactor, and the interpretation of preliminary experimental data by comparison with results of simulation and parameter estimation methods to demonstrate the validity of the design principles.

We refer to this design as the *programmable CVD reactor concept* because of the potential real-time control of gas-phase composition across the wafer surface has for making possible novel operating modes. For example, this reactor design will enable single-wafer combinatorial experiments in which different materials can be created or different process conditions can be tested in a single experiment, producing the library wafer illustrated in Figure 2. In subsequent deposition runs, the reactor then can be reprogrammed to produce uniform films corresponding to one point on the library wafer without making any hardware adjustments. This mode of operation is made possible by the combination of the flexible design of the programmable reactor and model-based interpretation of the sensor and metrology data collected during the processing of the library wafer.

Reactor Design Principles

A common feature of all the CVD systems discussed in the previous section having the capability of controlling spatial variations in gas composition leaving the showerhead (for example, Moslehi et al., 1995; Theodoropoulos et al., 2000) is that the actuation capabilities are limited to 1-dimensional control in the radial direction. Furthermore, a characteristic common to these designs is the segment-to-segment interaction produced by the net flow of reactant gas across the wafer to the reactor chamber exhaust. For example, consider the simulation results presented in Figure 3; this simulation depicts the behavior of a showerhead 0.1 m in diameter (100-mm wafer) with a 0.01-m gap between the showerhead and wafer surface. Gas flow to each segment is set to 20 sccm (standard cubic centimeter per minute) [3.33×10^{-7} m^3/s at standard temperature and pressure (STP)] and consists of H_2 at 623 K and 5 Torr (666.4 Pa), representative operating conditions for W CVD processes. The concentration of tungsten hexafluoride (WF_6) in the middle segment is set at 1 wt % in H_2. The equations describing the steady-state gas flow were solved using a global spectral discretization technique where the basis functions correspond to eigenfunctions of heat equation in cylindrical coordinates. In our solution approach, the discretized momentum balance equations are solved iteratively for the two velocity components for a given pressure field; this velocity field is substituted into the continuity equation to define a residual function that is minimized in a Galerkin procedure by projecting the residual function onto the pressure field basis functions. The WF_6 species balance equation likewise is discretized and solved iteratively using a Galerkin projection method and a Jacobian-free formulation of a Krylov subspace iterative procedure. Converged solutions were found using fewer than 50 basis functions in each of the directions.

Using this simulation approach, we can observe that when carrier gas is injected through the center and outer annular region, and the deposition precursor species are injected through the middle annular injection port, the net convection across the wafer shifts the region where the precursor plume interacts with the wafer surface downstream, relative to the injection point (Figure 3, top). Therefore, the net flux across the wafer surface, inherent in the annual segmented showerhead designs, reduces the ability to accurately control gas-phase composition at the wafer surface (Figure 3, bottom).

As an alternative to reactor systems based on the annular segmented showerhead design, the programmable reactor system incorporates three new design features to improve the spatial control of gas-phase composition. The first is the development of a showerhead design consisting of an assembly of hexagonal showerhead subelements (segments) arrayed across the wafer surface. The reactant gas composition and feed rate is controllable within each segment, resulting in true two-dimensional control of gas composition across the wafer. The spatial resolution with which gas-phase composition can be controlled is determined by the size of showerhead segments.

The second new design feature is the recirculation of residual gas up through each segment of the showerhead; exhaust gases mix in a common exhaust volume above the showerhead honeycomb structure (Figure 1). When the total volumetric flow rate and other properties of feed gas to each segment are equal, the effect of this design feature is to create periodic flow

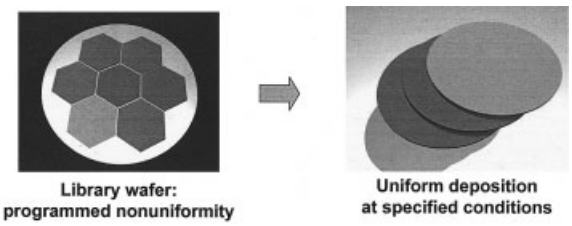

Figure 2. Rapid-process prototyping approach to new materials and process development.

The spatial patterning capabilities of the Programmable CVD reactor can be used to produce a "library" wafer (left) containing regions of distinct material properties; the reactor system then can be reprogrammed to deposit spatially uniform films of the chosen property (right).

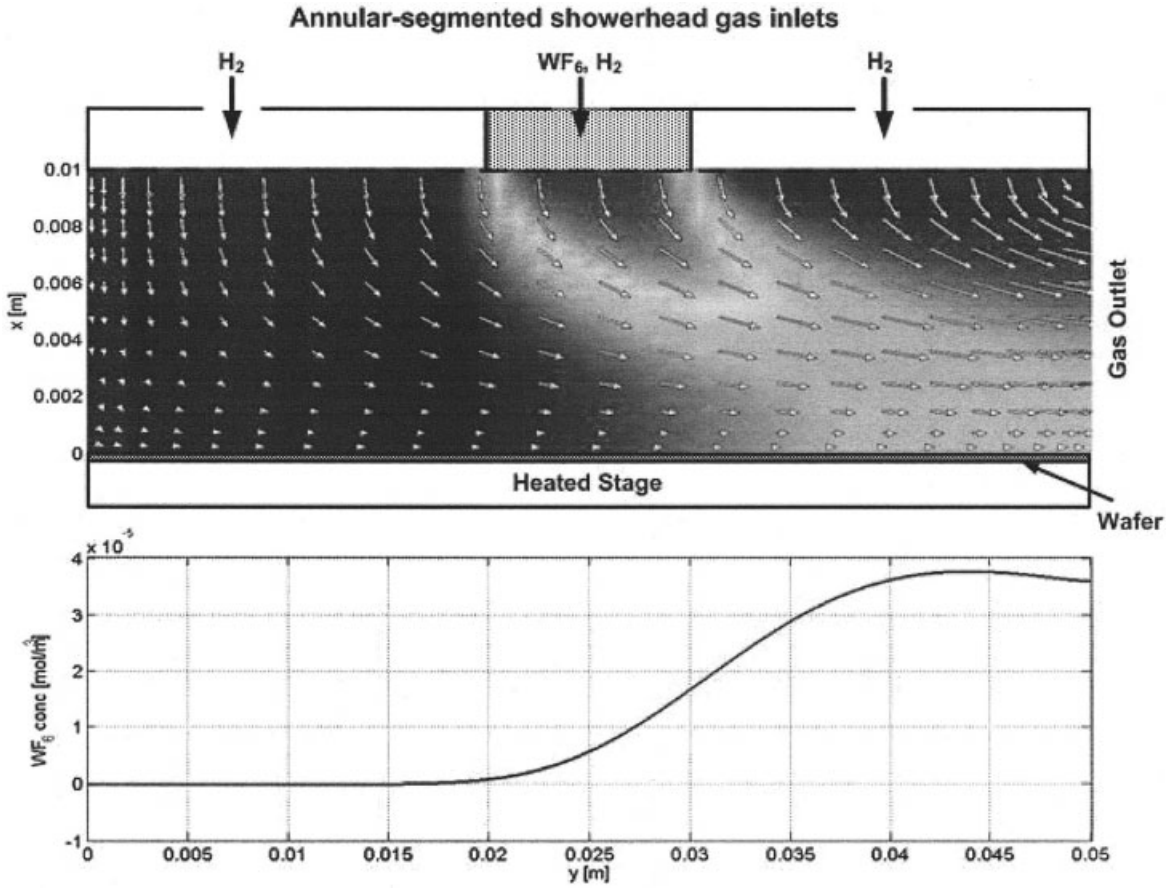

Figure 3. Gas concentration field computed for a segmented showerhead design.

The mismatch between gas injector location (top) and the resulting gas concentration profile over the wafer surface (bottom) in a non-reverse-flow design is illustrated.

fields in the gap region between the bottom of the showerhead assembly and the wafer surface (Figure 4). In this simulation result it is possible to see that the boundaries of the periodic flow field match the segment wall locations, indicating that there will be no convective flux of reactant species between the segment regions, eliminating the problems generated by drawing exhaust gas across the wafer surface. This simulation represents three segments in a linear arrangement with 20 sccm (3.33×10^{-7} m^3/s at STP) flow of H_2 to each; the simulation is limited to the gap region and does not take into account back-diffusion from the common exhaust volume. As in the simulation of the annular segmented showerhead design, the center segment also includes 1 wt % WF_6. Each segment has a diameter of 0.05 m, and each feed tube has a radius of 0.005 m. As in the annular design, $T = 623$ K and the total pressure was set to 5 Torr (666.4Pa). The numerical solution procedure for computing the gas velocity and composition fields, based on a global spectral projection method, is identical to that described for the annular geometry reactor.

The third new design feature of the programmable reactor is the ability to manipulate the shower-head/wafer gap size. Small gap settings will reduce intersegment diffusion in the gap region leading to deposition of distinct hexagonal patterns; increasing the gap size will spread the pattern, ultimately producing smooth concentration gradients across the wafer surface when reactant gas composition varies from segment to segment. An example of the smooth concentration gradients across the wafer surface that can be produced in this manner is shown in the simulation results depicted in Figure 4, where the across-wafer concentration profile of the WF_6 reactant species is shown.

Elimination of intersegment region convective transport in the gap improves the accuracy with which gas composition can be controlled across the wafer surface because across-wafer transport will be governed solely by diffusion. Likewise, the accuracy of simulators used to interpret deposition data will be enhanced, improving the ability to correlate process operating conditions with film properties at all points on the library wafer. Because of the potential for accurately predicting the continuous variation of gas-phase concentration across the wafer surface, it may be possible to generate library wafers with continuously graded characteristics across the wafer surface, increasing the information that can be obtained from a single deposition run. The system then can be run with closer showerhead-wafer spacing to produce a finite number of hexagonal patches of material selected from the first library wafer, to provide a more accurate assessment of the process conditions needed to produce the desired material.

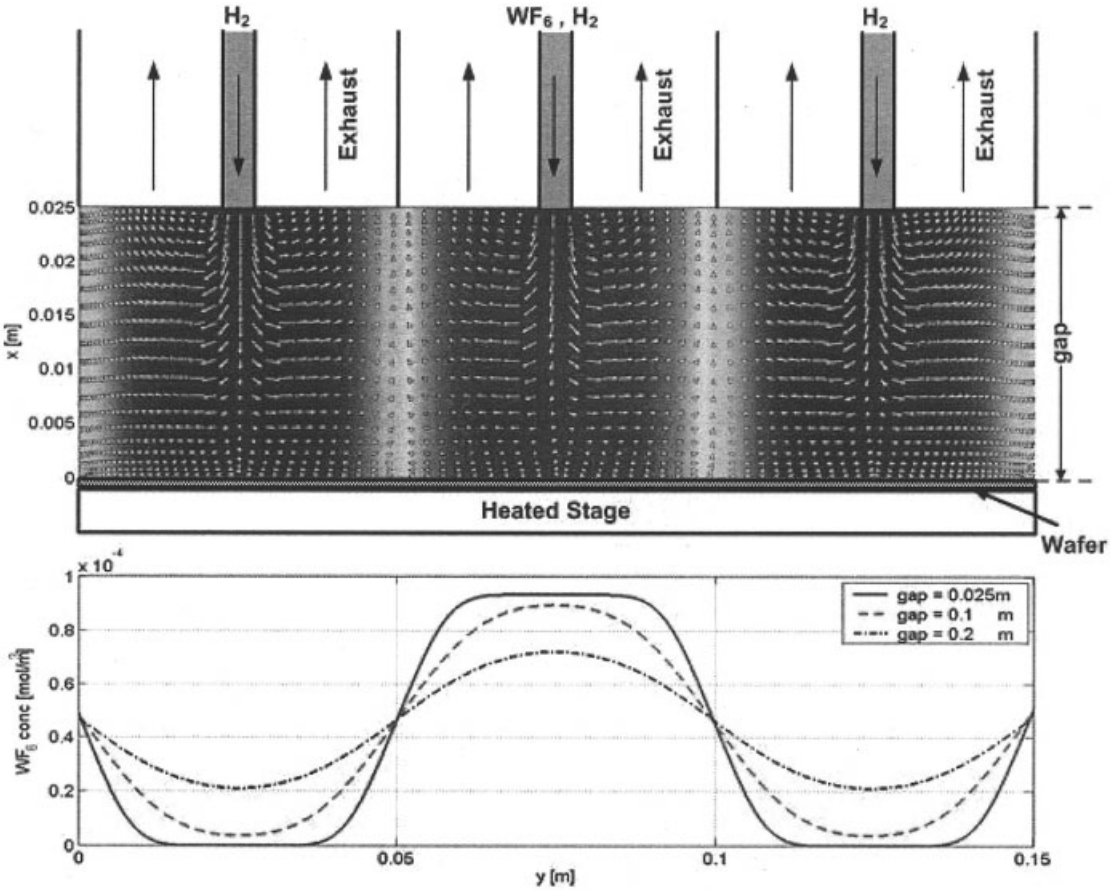

Figure 4. Periodic flow patterns and gas concentration field generated by a three segment, reverse-flow showerhead design (top) and resulting concentration profiles across the wafer as a function of gap size (bottom).

Prototype construction

To test the feasibility of the programmable CVD concept, a prototype reactor was designed and constructed by modifying one reaction chamber of an Ulvac-ERA1000 CVD cluster tool. The Ulvac cluster tool (located on the University of Maryland's campus) is a commercial CVD system used for selective W deposition. W CVD, used to form vertical interconnects in very large scale integration (VLSI) and ultralarge scale integration (ULSI) circuits, represents a relatively mature, but commercially important, manufacturing process (Ireland, 1997), and so was chosen for evaluating the engineering design of the programmable reactor. Although W CVD deposition mechanisms and reactor systems have been studied extensively (for example, Arora and Pollard, 1991; Kleijn, 2000; Kleijn and Werner, 1993; Kleijn et al., 1991), open process development issues remain. Even in the simplest case of blanket deposition using H_2 and WF_6, the reactant/reducing gas ratio and WF_6 gas concentration result in two operational degrees of freedom that force a trade-off between film conformality and deposition rate, where the latter is compounded by reactor design factors that determine where the transition from reaction rate to mass-transfer limited operation takes place.

In its original configuration, the hydrogen-reducing gas entered through a quartz showerhead above the wafer; wafer heating was provided by a ring of heating lamps above the showerhead. As part of the programmable reactor modifications, substrate heating was used in place of lamp heating, and the quartz showerhead was replaced by the new programmable reactor showerhead assembly. The primary component of the assembly is the honeycomb-shaped array of three segments machined from a single block of stainless steel. Each side of the hexagonal segments is $W = 25.4$ mm in length and the overall length of the honeycomb segment structure is $L = 144.08$ mm. As designed, the three segments cover most of the surface area of the 100-mm wafers used in deposition experiments. The segment length was made as long as physically possible subject to the constraints imposed by clearances necessary to insert the wafer and to prevent obstruction of the exhaust ports in the showerhead chamber.

Each segment is fitted with two 6.35-mm-ID feed tubes and one sampling tube (Figure 1). The feed and sampling tube vertical positions can be adjusted when the reactor is not operating. The sampling tube of each segment can be used to transport a small amount of gas to a real-time in situ sensor, such as a mass spectrometer. From the residual gas analysis of each segment, approximate film thickness and the composition of film deposited on each area corresponding to each segment can be determined (Gougousi et al., 2000).

Individual mass flow controllers with a range of 0–100 sccm ($0–1.667 \times 10^{-6}$ m^3/s at STP) were used to control the total flow of H_2, Ar, and WF_6 to the showerhead; a network of needle valves was used to split these gas flows to each show-

erhead segment. Showerhead/wafer spacing is controlled with the linear motion device shown in Figure 1. In addition to controlling intersegment region diffusion, the linear motion device is needed to raise the honeycomb structure sufficiently to allow the cluster tool's robot arm to insert and withdraw the wafer from the reactor chamber.

Modeling and Simulation

Because of the programmable CVD reactor's reverse-flow design, reactants in the gas mixture in the common exhaust volume can diffuse back into the segments. Therefore, to sustain the prespecified gas compositions at the bottom of each segment, the back-diffusion through the segments should be suppressed below an acceptable level by the convective upward flux contribution to species transport in each segment. A steady-state one-dimensional segment model (for each segment), combined with a well-mixed common exhaust volume model and a model of intersegment transport in the gap region between the wafer and showerhead segments for nonzero gap size, is developed in this section. The geometry of a single segment, together with the notation used in the model development, is shown in Figure 1.

This model was used to determine feed gas flows to the individual segments and to interpret preliminary experimental observations. In particular, the simulator was used to assess the ability of the segmented structure to maintain significant segment-to-segment gas composition differences near the wafer surface when the reactor was operated under the extreme condition of supplying pure Ar to segment 1, pure WF_6 to Segment 2, and pure H_2 to Segment 3.

Exhaust volume

As the first step in developing a model of reactant transport through each segment (Figure 1) and between each segment in the wafer/showerhead gap region, the mole fraction of each species denoted as

$$x_i^k(z) \qquad i = \mathrm{H_2}, \mathrm{WF_6}, \mathrm{Ar} \qquad k = 1, 2, 3 \qquad 0 \le z \le L$$

where the subscript i refers to the gas species and k is the segment number.

For this simulation study, the common exhaust volume was treated as perfectly mixed. Because of the relatively low depletion rate of the deposition reaction under the chosen operating conditions (this assumption will be validated later), the exhaust volume composition x_i^{exh} was computed simply as the average of the feed compositions to each segment.

Intersegment diffusion

The rate of across-wafer chemical species transport is determined by the gap size h between the honeycomb showerhead structure and wafer surface and the composition differences between the reactant gases at the bottom of each segment and the chamber itself. A simplified model of intersegment transport in this gap region can be derived for the experiment where pure gases are fed to each segment. For example, the flux of Ar from segment region 1 (where it is the primary feed gas) to segment 3 (where H_2 is the primary feed) can be written as

Table 1. List of Variables and Parameters

Symbol	Units (and Value)	Description
A_f	9.5×10^{-5} m^2	Feed + sample tube cross-sectional area
A_s	0.0016 m^2	Segment cross-sectional area
C	mol/m^3	Total concentration
D	m^2/s	Diffusivity of Si in W
D_{ij}	m^2/s	Gas-phase binary diffusion coefficient
D_i^T	kg/(ms)	Gas-phase thermal diffusion coefficient
f_d		Intersegment transport correction factor
h	m	Wafer/segment-bottom gap size
K^k	nm/min	W deposition rate coefficient
L	0.144 m	Segment length
M_i	kg/mol	Species i molecular weight
N_i^k	mol/(m^{2}s)	Species i segment k, total molar flux
$\bar{N}_i^k$	mol/(m^{2}s)	Species i segment k, ordinary diffusion flux
Q_i^k	m^3/s	Segment k, feed flow rate of species i
s_w	m	W film thickness
t	s	Time
T	K	Segment gas temperature
W	0.025 m	Segment side length
x_i^k		Species i segment k, mole fraction
z	m	1D segment coordinate
z_f	0.0508 m	Feed tube outlet location
ρ_i	kg/m^3	Pure species gas density

$$N_{\mathrm{Ar}}^{1-3} = CD_{\mathrm{Ar,H_2}} f_d \frac{x_{\mathrm{Ar}}^3(0) - x_{\mathrm{Ar}}^1(0)}{2W\cos(\pi/6)} \tag{1}$$

where the length scale of the finite-difference approximation to the composition gradient is the distance from the center of one hexagonal segment to the center of the adjacent segment. The flux correction factor f_d will be estimated from experimental data later in this paper. Because the chamber gas-phase composition could not be measured in the experiments discussed herein and because of the likelihood of WF_6 depletion arising from heated reactor components, transport between segment regions and the outer chamber is not included in this simulation study. The binary diffusion coefficients D_{ij} are estimated by the Chapman–Enskog kinetic theory and Neufield method (Kleijn and Werner, 1993; Reid et al., 1987). C is the total gas concentration. A complete summary of the parameters and variables used is presented in Table 1.

These values of intersegment species flux then are used as the initial value of the intrasegment flux terms

$$N_i^k(z) = \frac{hW}{A_s} \sum_{n=1}^{3} N_i^{k-n} + F_i^k(z)$$

where F_i^k is a function accounting for the change in flux attributed to fresh feed of species i from the segment feed tubes and is defined by

$$F_i^k = 0 \qquad z < z_f$$

$$F_i^k = Q_i^k \rho_i / [M_i(A_s - A_f)] \qquad z \ge z_f$$

where Q_i^k is the volumetric flow rate of gas species i to segment k.

Intrasegment transport

Neglecting any effect of pressure and forced diffusion, the multicomponent gas species transport can be expressed by the Maxwell–Stefan equation

$$\nabla x_i^k = \sum_{j=1}^{n} \frac{1}{CD_{ij}} (x_i^k N_j^k - x_j^k N_i^k) + \sum_{j=1}^{n} \frac{x_i^k x_j^k}{D_{ij}} \left(\frac{D_j^T}{\rho_j} - \frac{D_i^T}{\rho_i} \right) \nabla \ln T \qquad 0 < z < L$$

subject to boundary conditions

$$x_i^k(L) = x_i^{exh} \tag{2}$$

The gas temperature profile along the segment length z is needed to compute the contribution of thermal diffusion; observation of the W film deposited on the segment structure after a number of experimental runs indicates that there is significant gas and segment heating along the bottom-most third of the honeycomb segments. Given this observation, and the difficulty of obtaining accurate gas temperature measurements at low pressure, the gas temperature was approximated as a linear interpolation between the wafer (maintained at 350°C) and the ambient temperature (30°C) over the bottom third of the segment, and was set as the ambient temperature for the remainder of the segment.

The flux arising from ordinary diffusion can be defined as

$$\bar{N}_i^k = N_i^k + \frac{D_i^T}{M_i} \nabla \ln T$$

giving the simplified form of the Maxwell–Stefan equation

$$\nabla x_i^k = \sum_{j=1}^{n} \frac{1}{CD_{ij}} (x_i^k \bar{N}_j^k - x_j^k \bar{N}_i^k) \tag{3}$$

subject to boundary conditions in Eq. 2. The D_i^T are the multicomponent thermal diffusion coefficients computed using the correlations given in Kleijn and Werner (1993).

Simulation Results

The nine intersegment flux equations (Eq. 1) are solved simultaneously with the nine collocation-discretized Maxwell–Stefan equations (Eq. 3) subject to boundary conditions (Eq. 2) using a Newton–Raphson method to obtain the gas composition profiles as a function of position within each segment. Twenty collocation points located at the zeros of 19th-degree Chebyshev polynomial, plus the interval endpoints, were used to define the discretization arrays (Adomaitis, 2002).

Because the modeling equations for each segment are identical in structure and vary only in terms of parameter values, an object-oriented approach was taken to setting up the simulator: a segment model class (in MATLAB) was derived from an abstract class defining the general structure of a nonlinear algebraic equation model. Methods for the nonlinear equation model class included a Newton–Raphson-based equation solver, which is inherited by the segment model class. Because each segment model is an instance of the latter class, this approach is an efficient method for setting up models of this form, and is readily extensible to programmable reactor models with many more segment elements. More details on the computational approach will be given in a future report.

Representative results of this solution procedure are shown in Figure 5. In this figure, the wafer surface is located at $z = 0$ (the left axis limit) and the segment top is to the right; the vertical line represents the location z_f of the bottom of the feed tube bundle inside each segment. Two sets of simulations were performed to assess the effect total gas flow to each segment has on the composition profiles, and the results are discussed below. In each case, the gap size h was set to 0. Simulations to evaluate the effect of gap size h are presented later, to interpret some of the experimental findings.

Low-flow results

Simulator predictions for the gas composition profiles of Segments 1 to 3 (ordered from the top plot) for a gas feed flow of $Q = 2.5$ sccm (4.167×10^{-8} m^3/s at STP) to each segment are shown in the left column of plots in Figure 5. The composition in each segment as $z \rightarrow L$ approaches the composition of the gas in the common, well-mixed exhaust chamber. As the profiles are followed down the segments, the feed gas species of each segment becomes the primary component. However, because of the relatively low flow, significant back-diffusion of the other components occurs, resulting in a significant fraction of each species being found near the bottom of each segment: this is particularly true in Segment 3 because of the larger fraction of H_2 and the larger values of binary diffusion coefficients when H_2 is one of the species. It is also interesting to observe the effect thermal diffusion has in this simulation in each case: the region near the wafer is enriched in H_2 relative to the heavier species because of thermal diffusion. Thus, because of the large negative effects ordinary and thermal diffusion have on the ability to control gas composition near the wafer surface, it is possible to conclude that higher feed flow rates should be used.

High-flow results

Increasing the gas flow rate to 50 sccm (8.333×10^{-7} m^3/s at STP) in each segment has a dramatic effect on the gas composition profiles in each segment. As can be seen in the right column plots of Figure 5, the feed species to each segment becomes the dominant gas-phase species near the wafer surface. Thermal diffusion effects still can be observed, but have a much lower impact on the composition profiles. Under these operating conditions, the effect of changing the gap size on gas composition near the wafer surface should be more pronounced, and so initial experiments were conducted at these conditions. It should be noted that, although the WF_6 concentration at the bottom of Segments 1 and 3 is very small, it is nontrivial and so can (and does) result in film deposition under these segments.

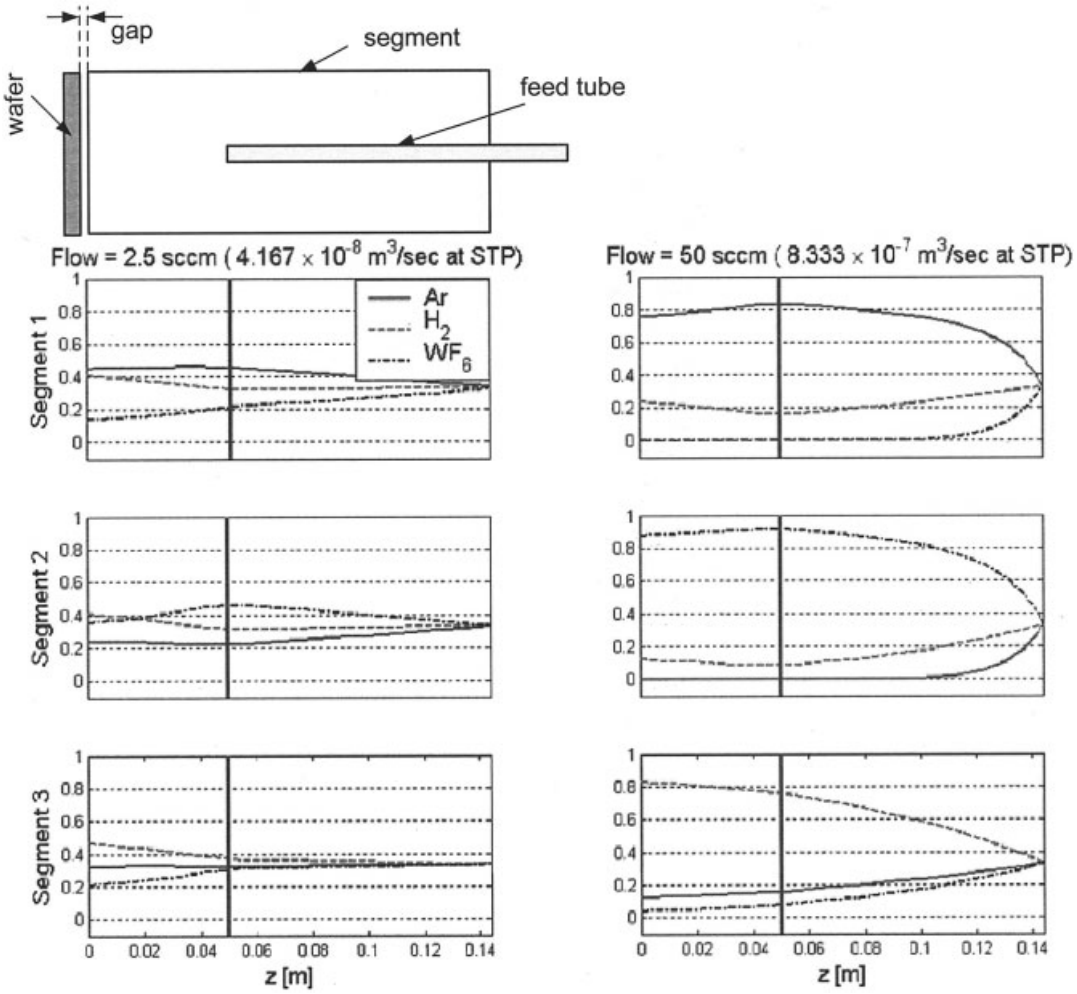

Figure 5. Gas composition profiles in each segment for two different gas flow rates for the Ar-fed segment (top), WF_6-fed segment (middle), and H_2-fed segment (bottom).

The vertical line marks the feed tube bundle outlet location.

Prototype Experimental Tests

Initial experiments were performed using the three-zone prototype to validate two basic programmable reactor design concepts: (1) that the reverse-flow showerhead design could maintain significant segment-to-segment gas-phase compositional differences near the wafer surface and (2) that spatially patterned wafers could be produced by this reactor design and that some of the characteristics of the pattern can be controlled by manipulating the showerhead/wafer gap. Typical operating conditions for the first experiments consisted of a 66.662 Pa chamber pressure, a wafer temperature of 350°C, and 10- to 20-min deposition times. The film thickness in the region below each segment was determined by sheet-resistance measurements using a four-point probe.

Segment-to-segment gas composition differences

In the set of experiments discussed herein, pure Ar was fed to Segment 1 at a flow rate of 8.333×10^{-7} m^3/s at STP; 8.333×10^{-7} m^3/s at STP of WF_6 was fed to Segment 2; and 8.333×10^{-7} m^3/s of H_2 was fed to Segment 3. Sheet-resistance measurements were made at seven points on the

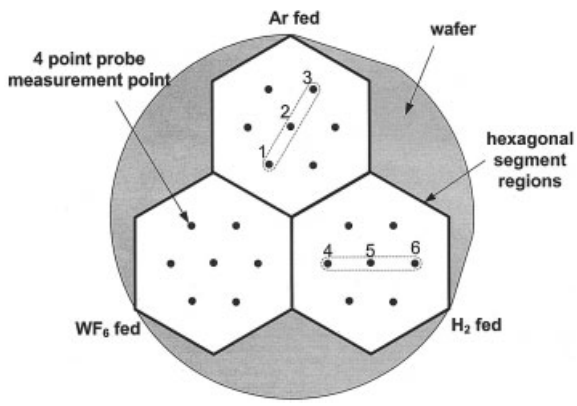

Figure 6. Film thickness measurements point locations (determined by sheet resistance measurements) relative to segment locations.

Seven measurements were made in each segment region.

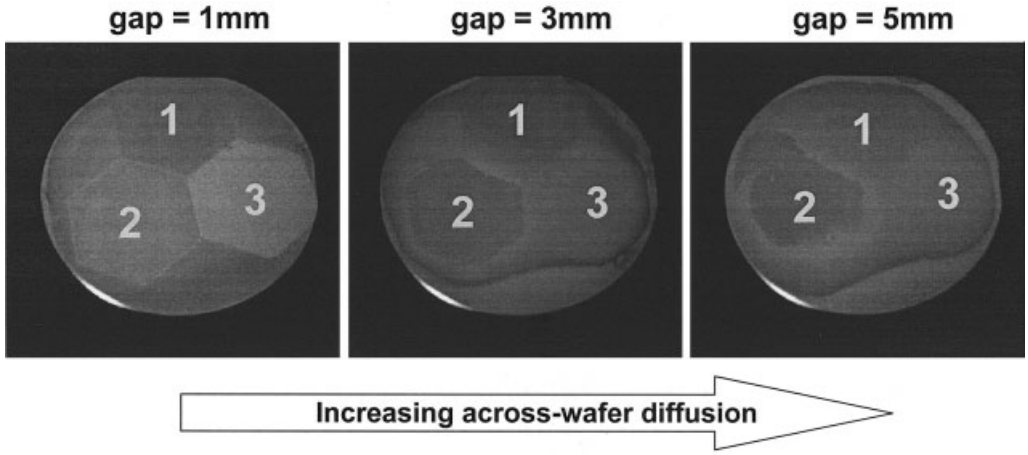

Figure 7. Deposition patterns produced using three different values for the showerhead/wafer gap spacing.

In these experiments, pure Ar, WF_6, and H_2 were fed to the individual segments.

wafer surface in each segment region; locations of the data points are shown in Figure 6. Simulator predictions for these conditions indicate that the gas composition at the wafer surface is mainly the segment-feed species, with a small amount of WF_6 present at the bottom of segments even when $h = 0$ (Figure 5). Although W deposition should take place directly under Segment 2 (where pure WF_6 is fed) because of the Si-reduction mechanism, it is interesting to note that some W deposition takes place under the remaining two segments. Experimental data and simulator predictions in the remainder of this paper will validate that the WF_6 responsible for deposition in Segments 1 and 3 is transported to this region through a combination of back-diffusion and intersegment diffusion.

Control of pattern resolution

In all cases where the showerhead/wafer spacing was small (such as $h = 1$ mm), distinct hexagonal film patterns were produced (Figure 7). As the gap is increased, the contribution of back-diffusion down the segments from the common exhaust remains essentially constant, whereas intersegment diffusion in the gap region increases. Photographs of wafers processed for three different gap values are shown in Figure 7, demonstrating that the pattern becomes more diffused with increasing gap size. This decrease in the sharpness of the deposition pattern provides visual evidence for the effectiveness of using gap size to control intersegment diffusion of reactant species across the wafer surface.

Across-wafer diffusion of WF_6 from Segment 2 to the Ar- and H_2-fed segments should result in a negative film thickness gradient along lines drawn through the latter two segments in the direction away from Segment 2 (as seen in the two sets of measuring points: 1, 2, and 3 for Ar-fed segment; and 4, 5, and 6 in H_2-fed segment in Figure 6). This is clearly evident in the linear interpolation plots presented in Figure 8, where the film thickness along these two "cuts" in Segments 1and 3 is plotted for three different values of gap size. Furthermore, we observe the overall thickening of the film in these two segments as the gap increases, a phenomenon attributable to the increased WF_6 concentration resulting from increasing intersegment diffusion as the gap is increased. Likewise, extrapolating the growth rates of Segments 1 and 3 to $h = 0$ (which is an undesirable experiment to perform) shows positive growth rates in each segment for zero gap, indicating the contribution of intrasegment back-diffusion of WF_6 to the growth rate in each of these segments. It is interesting to note the greater slope of the deposition rate line in Segment 1 relative to that of Segment 3; this may be attributable to the smaller binary diffusion coefficient in the Ar–WF_6 mixture compared to that in the H_2–WF_6 mixture.

Finally, error bars indicating the standard deviation of all seven sheet-resistance measurements per segment are plotted; the slightly increasing trend with gap size may indicate additional effects of intersegment and chamber-segment diffusion on film thickness variation within each segment region as the gap increases. For increasing values of very large values of h (such as <10 mm), the variability should begin to decrease with h because of the dominance of across-wafer diffusion under these operating conditions.

Simulation-Based Interpretation of Film Deposition Results

Thin films of tungsten can be deposited in either a selective or blanket tungsten deposition mode. The gas-phase reactions associated with these deposition processes are negligible as a result of low reactor pressure during the process operation (Arora and Pollard, 1991; Kleijn et al., 1991); thus the deposition rate is determined only by surface reaction and chemical species transport rates in the gas/wafer surface interface and through the deposited film itself. The overall reaction of tungsten deposition by hydrogen reduction on a silicon wafer substrate begins with surface reactions by Si reduction during the film nucleation step; the reaction is

$$2WF_6(g) + 3Si(s) \rightarrow 2W(s) + 3SiF_4(g)$$

in the range of deposition temperature used in our experiments (Leusink et al., 1992). Numerous studies have focused on the extent to which this reaction takes place and when the transition to the H_2 reduction process

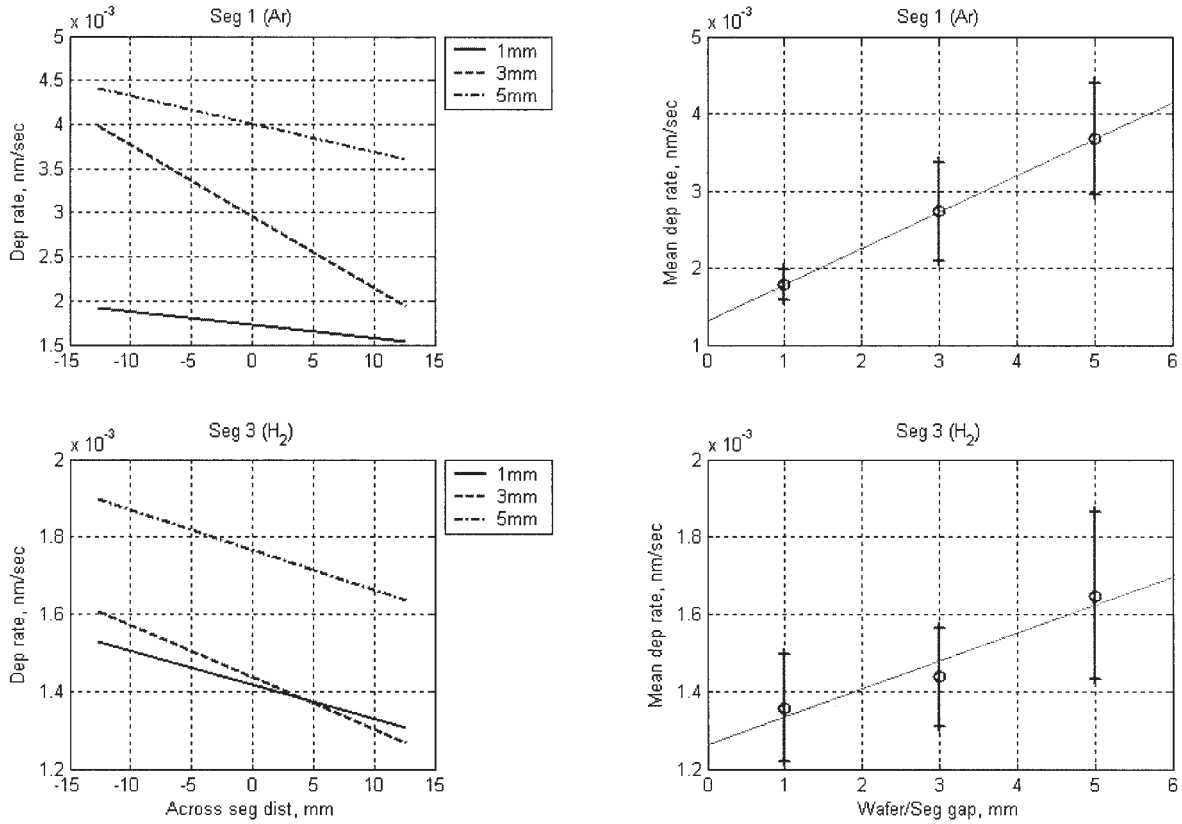

Figure 8. Film thickness measurements for three showerhead/wafer spacing values showing how film thickness decreases in the Ar- and H_2-fed segments with distance from the WF_6 segment (left) and how overall film thickness increases in each segment region as the spacing is increased (right).

$$WF_6(g) + 3H_2(s) \rightarrow W(s) + 6HF(g)$$

occurs. Most studies conclude the Si-reduction step is self-limiting and typically accounts for 10–200 nm of W film thickness at the Si substrate/W film interface (Groenen et al., 1994). However, Joshi et al. (1992) presented a counterexample study in which non-self-limited growth was observed using two different CVD systems, resulting in relatively thick W films. A mechanism for this deposition process was proposed whereby Si out-diffused from the substrate through the deposited W film and reacted with WF_6 on the film surface; this process was found to be promoted by oxygen impurities in the W film. The expression for the overall deposition rate was determined to depend on the product of the film surface Si concentration and the gas WF_6 concentration at the film surface, as follows

$$N_{Si}\frac{ds_w}{dt} = R_k C_i$$

(after Eq. A5 in Joshi et al., 1992), where N_{Si} is the number density associated with the growing film scaled by the number of Si moles required to produce 1 mole of W film, and s_w is the film thickness. The first term in this product is attributable to the surface reaction, which is nth order in WF_6

$$R_k = K_0 e^{-E_a/RT}[Cx_{WF_6}]^n \tag{4}$$

The second term is derived from the assumption that Si transport through the W film is governed by Fick's Law; a finite-difference approximation to the diffusion flux, together with the assumption that the diffusive flux is in equilibrium with the surface reaction above, gives the term associated with the surface Si concentration as

$$C_i = \frac{C_0}{1 + K_0 s_w [Cx_{WF_6}]^n e^{-E_a/RT}/D}$$

where C_0 is the concentration of Si in the W film at the W/Si interface and D is the diffusion coefficient of Si in W. [See Joshi et al. (1992) for a more detailed derivation of these rate expressions.] For short deposition times or thin films ($s_w \rightarrow 0$) produced by low deposition temperature or low WF_6 concentration, $C_i \rightarrow C_0$ and the deposition rate is determined only by the surface reaction rate R_k (in the absence of gas-phase transport limitations); thus

$$\frac{ds_w}{dt} = \frac{C_0 K_0}{N_{Si}} e^{-E_a/RT} C^n [x_{WF_6}]^n \tag{5}$$

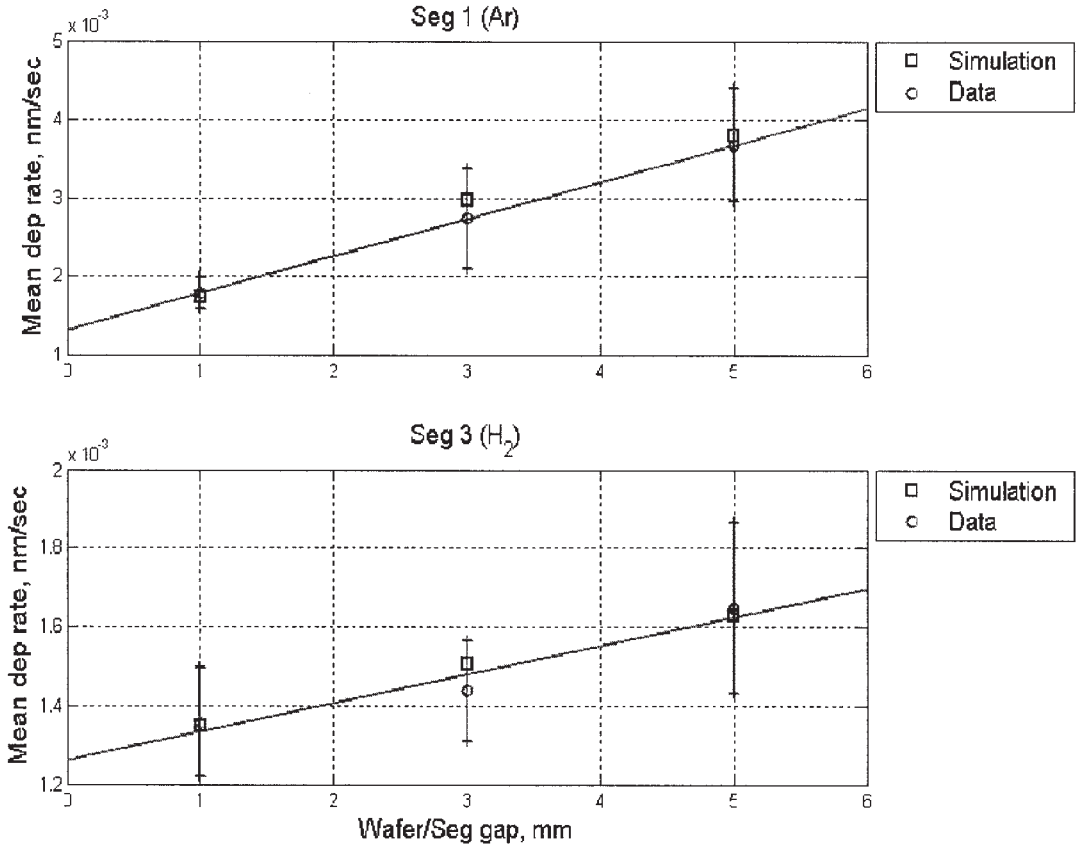

Figure 9. Simulated predictions of the W deposition rate by Si reduction in the Ar- and H_2-fed segments compared to experimental measurements.

Simulated vs. measured deposition rates

Simulation of the deposition process in Segments 1 and 3 can be used as an indirect method to quantify the rate of intersegment transport in the wafer/showerhead gap region. This will be carried out by estimating the parameter f_d in Eq. 1 and the reaction rate coefficients $K^k(T)$ in the simplified rate expression (Eq. 5) for growth of very thin films by Si reduction in segments $k = 1$ and 3

$$\frac{ds_w^k}{dt} = K^k[x_{WF_6}^k(0)]^n$$

where

$$K^k = \frac{C_0 K_0}{N_{Si}} e^{-E_a/RT} C^n$$

Simulations were performed using the three-segment reactor model for gap values of $h = 1$, 3, and 5 mm and a fixed value of f_d to obtain the values of $x_{WF_6}(0)$ for segments $k = 1$ and 3. Because Si reduction depends on the surface condition of the silicon wafer, a least-squares fit of the rate coefficients K^k to the experimentally measured rate data was performed for each segment instead of using a constant value for all segments; the optimal value of f_d was determined by minimizing the error in this regression. This approach is not inconsistent with Joshi et al. (1992), where parameter fitting was used to determine the reaction rate preexponential constant K_0 and the activation energy E_a. The parameter values obtained using this estimation method are

$$f_d = 0.2 \qquad K^1 = 1.92 \text{ nm/min} \qquad K^3 = 0.36 \text{ nm/min}$$

Simulator predictions of growth rates as a function of h are compared to experimental data in Figure 9. That a good fit is obtained for the rate exponent of $n = 0.5$ (recommended by Joshi et al., 1992) is significant because an accurate rate description for rates linear in WF_6 concentration and that pass through $ds_w/dt = 0$ for $x_{WF_6} = 0$ could not be found for these data. The different values of K^k determined for each segment can be attributed to the different wafer surface temperatures in each segment as a result of gas composition differences (Chang et al., 2001) or film surface condition differences resulting from the H_2/Ar composition differences.

The resulting simulator predictions are consistent, qualitatively as well as quantitatively, with the observed reactor behavior, indicating the importance of intrasegment backdiffusion and intersegment diffusion across the wafer surface in governing the observed deposition rates, and how these processes can be controlled by adjusting the gap size and feed gas flow rate in this reactor design. Finally, in Table 2, the magnitude of gas species fluxes arising from bulk flow up the segment, the (gas-phase) diffusion pro-

Table 2. Comparison of Fluxes Predicted by the Reactor Simulator

Flux	Value, mol/(m^{2}s)
Convective (F_i^k)	O (10^{-2})
Intra- and intersegment (N_i^{j-k})	O (10^{-5})
Deposition rate	O (10^{-7})

cesses, and the deposition rate are compared to justify the original assumption that the deposition rate is low compared to that of the transport processes and could be neglected in the original derivation of the reactor segment model.

Conclusions

A new approach to designing spatially controllable chemical vapor deposition reactors was presented herein. The primary design innovation of this CVD system was the introduction of a segmented, reverse-flow gas delivery (showerhead) assembly. A three-segment prototype reactor was constructed to prove the validity of the design concept and provide engineering data for simulator development. Preliminary experimental testing demonstrated the validity of the design by depositing spatially patterned films using the reactor's ability to control across-wafer gas composition. Simulation studies were performed to interpret experimental data and to estimate gas-phase composition at the wafer surface.

This approach to thin-film manufacturing control opens the door to a new generation of CVD reactor designs, allowing single-wafer combinatorial studies and precise across-wafer uniformity control in a single reactor design. The modular nature of the showerhead segments offers the possibility of developing CVD reactors for very large substrates. To reach these goals, a new reactor is under construction that includes a more precisely controllable reactant gas delivery system, a cleaner reaction chamber environment, and better access to the wafer while the deposition process is taking place. It is anticipated that the additional instrumentation in the next prototype will allow a demonstration of the programmability capabilities envisioned for this system. Research in improving the manufacturability of the showerhead segment modules, particularly integrating feed gas flow control into each segment, is also in progress.

Acknowledgments

The authors acknowledge the support of the National Science Foundation (NSF) through Grant CTS-0085632 for construction of the prototype and simulation work, the continued support of NSF through CTS 0219200, and National Institute of Standards and Technology for fabricating several showerhead components. The assistance of Jing Chen in several aspects of the simulation work also is acknowledged.

Literature Cited

Adomaitis, R. A., "Objects for MWR," *Comput. Chem. Eng.*, **26**(7–8), 981 (2002).

Arora, R., and R. Pollard, "A Mathematical Model for Chemical Vapor Deposition Process Influenced by Surface Reaction Kinetics: Application to Low-Pressure Deposition of Tungsten," *J. Electrochem. Soc.*, **38**(5), 1523 (1991).

Banks, H. T., S. C. Beeler, G. M. Kepler, and H. T. Tran, "Reduced Order Modeling and Control of Thin Film Growth in an HPCVD Reactor," *SIAM J. Appl. Math.*, **62**, 1251 (2002).

Chang, H.-Y., R. A. Adomaitis, J. N. Kidder, Jr., and G. W. Rubloff, "Influence of Gas Composition on Wafer Temperature in a Tungsten Chemical Vapor Deposition Reactor: Experimental Measurements, Model Development, and Parameter Estimation," *J. Vac. Sci. Technol. B*, **19**, 230 (2001).

Christofides, P. D., *Nonlinear and Robust Control of PDE Systems: Methods and Applications to Transport-Reaction Processes*, Birkhäuser Verlag, Basel, Switzerland (2001).

Gadgil, P. N., "Optimization of a Stagnation Point Flow Reactor Design for Metalorganic Chemical Vapor Deposition by Flow Visualization," *J. Crystal Growth*, **134**, 302 (1993).

Gougousi, T., Y. Xu, J. N. Kidder, Jr., G. W. Rubloff, and C. R. Tilford, "Process Diagnostics and Thickness Metrology for the Chemical Vapor Deposition of W from H_2/WF_6 using In-Situ Mass-Spectrometry," *J. Vac. Sci. Technol. B*, **18**, 1352 (2000).

Groenen, P. A. C., J. G. A. Holscher, and H. H. Brongersma, "Mechanism of the Reaction of WF_6 and Si," *Appl. Surf. Sci.*, **78**, 123 (1994).

Ireland, P. J., "High Aspect Ratio Contacts: A Review of the Current Tungsten Plug Process," *Thin Solid Films*, **304**, 1 (1997).

Joshi, R. V., V. Prasad, M. L. Yu, and G. Scilla, "Non-Self-Limiting Nature of Silicon Reduction of WF_6 in Cold Wall Systems," *J. Appl. Phys.*, **71**(3), 1428 (1992).

Kepler, G. M., H. T. Tran, and H. T. Banks, "Reduced Order Model Compensator Control of Species Transport in a CVD Reactor," *Optim. Contr. Appl. Methods*, **21**, 143 (2000).

Kepler, G. M., H. T. Tran, and H. T. Banks, "Compensator Control for Chemical Vapor Deposition Film Growth Using Reduced-Order Design Models," *IEEE Trans. Semicond. Manuf.*, **14**, 231 (2001).

Kiether, W. J., M. J. Fordham, S. Yu, A. J. S. Neto, K. A. Conrad, J. Hauser, F. Y. Sorrell, and J. J. Wortman, "Three-Zone Rapid Thermal Processor System," *Proc. 2nd Int. RTP Conf.*, pp. 96–101 (1994).

Kim, B. N., and H. H. Lee, "Numerical Simulation of Metalorganic Chemical Vapor Deposition of Copper in a Single-Wafer Reactor," *J. Electrochem. Soc.*, **144**, 1765 (1997).

Kleijn, C. R., "Computational Modeling of Transport Phenomena and Detailed Chemistry in Chemical Vapor Deposition—A benchmark Solution," *Thin Solid Films*, **365**, 294 (2000).

Kleijn, C. R., C. J. Hoogendoorn, A. Hasper, J. Holleman, and J. Middelhoek, "Transport Phenomena in Tungsten LPCVD in a Single-Wafer Reactor," *J. Electrochem. Soc.*, **138**, 509 (1991).

Kleijn, C. R., Th. H. van der Meer, and C. J. Hoogendoorn, "A Mathematical Model for LPCVD in a Single Wafer Reactor," *J. Electrochem. Soc.*, **136**, 3423 (1989).

Kleijn, C. R., and C. Werner, *Modeling of Chemical Vapor Deposition of Tungsten Films*, Birkhäuser Verlag, Basel, Switzerland (1993).

Kobayashi, A., A. Sekiguchi, K. Ikeda, O. Okada, N. Hosokawa, Y. Tsuchiya, and K. Ueno, "The Deposition Rate for Cu CVD," *Advanced Metalization and Interconnect Systems for ULSI Applications*, R. Havemann, J. Schmitz, H. Komiyama, and K. Tsubouchi, eds., Materials Research Society, Pittsburgh, PA, pp. 177–183 (1997).

Leusink, G. J., C. R. Kleijn, T. G. M. Oosterlaken, C. A. M. Janssen, and S. Radelaar, "Growth Kinetics and Inhibition of Growth of Chemical Vapor Deposited Thin Tungsten Films on Silicon from Tungsten Hexafluoride," *J. Appl. Phys.*, **72**(2), 490 (1992).

Moffat, H. K., and K. F. Jensen, "Three-Dimensional Flow Effects in Silicon CVD in Horizontal Reactor," *J. Electrochem. Soc.*, **135**, 459 (1988).

Moslehi, M. M., C. J. Davis, and A. Bowling, "Single Wafer Thermal Processing and Wafer Cleaning," *TI Technical J.*, **Sep.–Oct.**, 44 (1992).

Moslehi, M. M., C. J. Davis, and R. T. Matthews, "Programmable Multizone Gas Injector for Single-Wafer Semiconductor Processing Equipment," U.S. Patent No. 5 453 124 (1995).

Reid, R. C., J. M. Praunitz, and B. E. Poling, *The Properties of Gases and Liquids*, 4th ed., McGraw-Hill, New York (1987).

Stuber, J. D., I. Trachtenburg, and T. F. Edgar, "Design and Modeling of Rapid Thermal Processing Systems," *IEEE Trans. Semicond. Manuf.*, **11**, 442 (1998).

Theodoropoulos, C., T. J. Mountziaris, H. K. Moffat, and J. Han, "Design of Gas Inlets for the Growth of Gallium Nitride by Metalorganic Vapor Phase Epitaxy," *J. Crystal Growth*, **217**, 65 (2000).

Theodoropoulou, A., E. Zafiriou, and R. A. Adomaitis, "Inverse Model Based Real-Time Control for Temperature Uniformity of RTCVD," *IEEE Trans. Semicond. Manuf.*, **12**, 87 (1999).
van der Stricht, W., I. Moerman, P. Demeester, J. A. Crawley, and E. J. Thrush, "Study of GaN and InGaN Films Grown by Metalorganic Chemical vapor Deposition," *J. Crystal Growth*, **170**, 344 (1997).
Wang, C. A., S. H. Gorves, S. C. Palmateer, D. W. Weyburne, and R. A. Brown, "Flow Visualization Studies of OMVPE Reactor Designs," *J. Crystal Growth*, **77**, 136 (1986).
Xia, L., P. W. Lee, M. Chang, I. Latchford, P. K. Narwankar, and R. Urdahl, "Chemical Vapor Deposition," *Handbook of Semiconductor Manufacturing Technology*, Y. Nishi and R. Doering, eds., Marcel Dekker, New York, Chapter 11 (2000).
Yang, C., C. Huang, G. Chi, and M. Wu, "Growth and Characterization of GaN by Atmosphere Pressure Metalorganic Chemical-Vapor Deposition with a Novel Separate-Flow Reactor," *J. Crystal Growth*, **200**, 39 (1998).

Manuscript received Aug. 4, 2003, and revision received Jun. 18, 2004.